GMR
The Original

GREEN SYNTHESIS OF ZINC OXIDE NANOPARTICLES USING *PHYLLANTHUS RETICULATUS* POIR. LEAF EXTRACT: STRUCTURAL, OPTICAL, MORPHOLOGICAL, AND ELEMENTAL CHARACTERISATION

Dr. T. Uma Kiran[1*], J. Swetha[2]

[1]Associate Professor of Botany, Girraj Government College (A), Nizamabad, Telangana, India.
[2]Girraj Government College (A), Nizamabad, Telangana, India

ABSTRACT
Plant-mediated routes to zinc oxide (ZnO) nanoparticles (NPs) are attractive because they avoid toxic reagents, but many reports support their structural and compositional claims only qualitatively. Here, ZnO NPs were prepared by alkaline precipitation of zinc acetate in the presence of an aqueous leaf extract of *Phyllanthus reticulatus* Poir., followed by washing, drying at 80 °C, and calcination, and were characterised by UV–Visible spectroscopy, FTIR, XRD, SEM–EDX, and TEM with SAED. XRD confirmed hexagonal wurtzite ZnO (JCPDS 36-1451) with refined lattice parameters a = 3.257 Å and c = 5.220 Å, no distinct reflections from secondary crystalline phases, and a mean Scherrer crystallite size of 10 ± 2 nm. The UV–Vis spectrum showed a band-edge shoulder at about 340–400 nm and a Tauc direct optical band gap of ≈3.18 eV. FTIR showed a strong Zn–O band at 565 cm^{-1}, along with O–H, H–O–H, and C–O bands from surface hydroxyl groups, adsorbed water, and residual organic matter. SEM showed sub-micrometre agglomerates of rounded grains, whereas TEM showed quasi-spherical primary particles of 15.3 ± 6.2 nm (n = 7) with resolved lattice fringes. SEM–EDX detected Zn and O with Zn:O atomic ratios of 0.46 and 0.41, i.e., oxygen-rich relative to stoichiometric ZnO, consistent with surface hydroxyl, adsorbed water, and organic residues. Because zinc was precipitated with NaOH, the extract is best viewed as a complexing, capping, and stabilising medium rather than a reducing agent. The results provide baseline structural data for *P. reticulatus*-derived ZnO and identify the additional measurements needed before application studies.

KEYWORDS: green synthesis; zinc oxide nanoparticles; *Phyllanthus reticulatus*; wurtzite; optical band gap; electron microscopy

1. INTRODUCTION
Nanotechnology underpins advances in medicine, agriculture, environmental remediation, catalysis, electronics and biotechnology (Mishra et al., 2017). At the nanoscale, materials show a high surface-area-to-volume ratio and optical, electrical, and catalytic properties that differ markedly from those of the bulk (Altammar, 2023). Among metal oxides, zinc oxide (ZnO) is a wide-band-gap semiconductor (≈3.37 eV at room temperature) with a large exciton binding energy (≈60 meV), good chemical stability and low toxicity, which has made it a model material for optical, sensing, photocatalytic and biomedical research (Özgür et al., 2005; Sirelkhatim et al., 2015).
ZnO nanoparticles are conventionally produced by sol–gel processing, hydrothermal synthesis, precipitation and thermal decomposition. These routes give good control over size and morphology but often need costly equipment, high energy input, or toxic reagents and stabilisers (Iravani, 2011; Kołodziejczak-Radzimska & Jesionowski, 2014). Green synthesis using plant extracts has therefore been proposed as a simple, economical and environmentally benign alternative (Agarwal et al., 2017). Plant extracts contain polyphenols, flavonoids, alkaloids, terpenoids, tannins, saponins, proteins and carbohydrates that can complex metal ions, adsorb on growing particles and limit their aggregation (Ahmed et al., 2016). The final product, however, is governed by synthesis parameters such as precursor concentration, pH, temperature, extract-to-precursor ratio and calcination conditions (Shaba et al., 2021), and the exact role of the extract depends on the route. When zinc is precipitated as the hydroxide with a base, Zn(II) is not reduced; ZnO forms by dehydration of $Zn(OH)_2$, and the biomolecules act mainly as complexing, capping, and stabilising agents.
Phyllanthus reticulatus Poir. (Phyllanthaceae) is a medicinal shrub widely distributed in tropical and subtropical Asia (Luo et al., 2011). It is used in traditional medicine and is reported to contain flavonoids, phenolic acids, tannins, lignans, alkaloids and terpenoids (Mugheri et al., 2023; Sahana et al., n.d.). Related *Phyllanthus* species have already been used to prepare biogenic ZnO nanoparticles (Sangeetha et al., 2026). To the best of our knowledge, however, a multi-technique characterisation of ZnO nanoparticles obtained with *P. reticulatus* leaf extract has not been reported. Characterisation is also where many green-synthesis reports are weakest: band gaps and crystallite sizes are often not quantified, energy-dispersive X-ray (EDX) results are over-interpreted, and spectra are assigned to phytochemicals without supporting controls (Mourdikoudis et al., 2018).
The present work therefore (i) prepares ZnO nanoparticles with *P. reticulatus* leaf extract by a precipitation–calcination route, (ii) characterises them by UV–Vis, FTIR, XRD, SEM–EDX and TEM/SAED, and (iii)

quantifies crystallite size, lattice parameters, optical band gap and elemental ratios, stating the limits of each technique explicitly.

2. MATERIALS AND METHODS

2.1 Plant material and chemicals

Healthy, disease-free leaves of P. reticulatus were collected from plants growing naturally in and around Girraj Government College (Autonomous), Nizamabad District, Telangana, India, on 15 July 2024. The plant was identified using standard regional floras and taxonomic keys, and a voucher specimen was deposited at GGCB/PR-2024/07. Zinc acetate dihydrate [Zn(CH3COO)2·2H2O], sodium hydroxide and absolute ethanol were of analytical-reagent grade, and double-distilled water was used throughout.

2.2 Preparation of leaf extract

Leaves were washed with running tap water to remove dust and soil, rinsed several times with distilled water, and blotted dry with filter paper. Twenty grams of chopped fresh leaves were heated in 100 mL of distilled water at 60–70 °C for 20–30 min with continuous stirring. After cooling to room temperature, the mixture was filtered through Whatman No. 1 filter paper, and the clear filtrate was stored at 4 °C until use.

2.3 Synthesis of ZnO nanoparticles

A 0.01 M solution of zinc acetate dihydrate (M = 219.5 g mol−1; 2.195 g L−1, i.e. 0.878 g per 400 mL) was prepared freshly in distilled water 0.878 g. Under magnetic stirring at room temperature, 100 mL of leaf extract was added slowly to 400 mL of the zinc acetate solution (extract : precursor = 1 : 4, v/v), and the mixture was stirred at 600 rpm for 30 min. The pH was then raised to 10–11 with 1 M NaOH, which precipitates zinc hydroxide that is converted to ZnO on heating:

$Zn^{2+} + 2\ OH^- \rightarrow Zn(OH)_2 \rightarrow ZnO + H_2O$

(Kołodziejczak-Radzimska & Jesionowski, 2014). The suspension was heated at 70 °C for 2 h with stirring, cooled naturally, and left undisturbed for 12–24 h. The white precipitate was collected by centrifugation (10,000 rpm, 15 min), washed 3 times with distilled water to remove residual acetate, sodium, and soluble organics, and then twice with absolute ethanol. The solid was dried in a hot-air oven at 80 °C for about 12 h to constant weight and calcined at 500 °C for 3 h in ambient air to give a fine white powder. The workflow is summarised in Fig. 1.

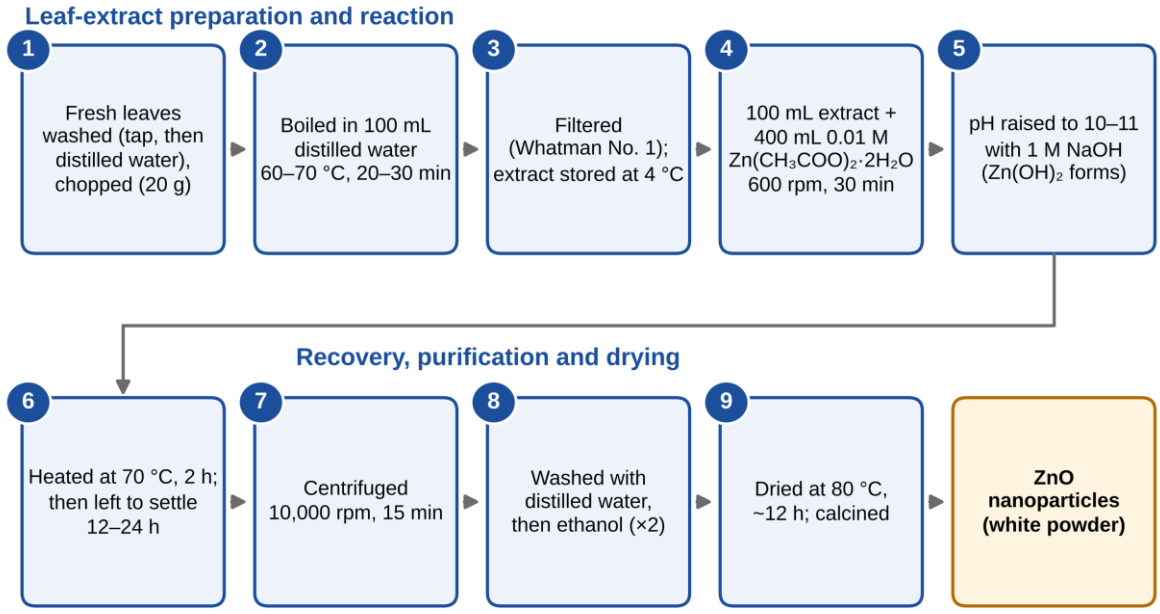


Fig. 1. Workflow for the synthesis of ZnO nanoparticles with *Phyllanthus reticulatus* leaf extract (steps 1–9; quantities as given in Section 2).

2.4 Characterisation

UV–Vis absorption spectra of the ZnO dispersion (distilled water (0.5 mg mL−1), sonicated for 10 min) were recorded from 200 to 800 nm on a JASCO V-770 spectrophotometer (1 nm data interval, 1.0 nm UV/Vis bandwidth, 1000 nm min−1; lamp change-over at 340 nm, grating change at 850 nm). The optical band gap was estimated from a Tauc plot, (Ahν)2 versus hν, for a direct allowed transition (Tauc et al., 1966), using absorbance A in place of the absorption coefficient and a linear fit over 3.30–3.65 eV (Makuła et al., 2018). FTIR spectra were collected from 4000 to 400 cm−1 (32 scans, resolution 8 cm−1, DTGS detector, KBr beamsplitter) on a Bruker Alpha FTIR spectrometer using the ATR mode. Because the resolution is 8 cm−1, band positions are reported to the nearest cm−1.

XRD patterns were recorded on a Rigaku Ultima IV X-ray diffractometer with Cu Kα radiation (λ = 1.5406 Å) radiation over 2θ = 5–80° (0.02° per step at 2° min−1). Peak positions and full widths at half maximum (FWHM) were obtained by pseudo-Voigt profile fitting. Crystallite size was estimated with the Scherrer equation, D = Kλ/(β

cos θ), with K = 0.9 and no correction for instrumental broadening, so the values are lower bounds (Patterson, 1939; Langford & Wilson, 1978). Lattice parameters a and c were refined by least squares from the nine indexed reflections using 1/d2 = (4/3)(h2 + hk + k^2)/a2 + l2/c2 with a zero-offset term. Texture coefficients were calculated relative to the JCPDS 36-1451 intensities.
Field-emission SEM images were acquired on a ZEISS instrument with an InLens detector at 5.0 kV accelerating voltage and working distances of 5.6–5.7 mm (50 k× and 200 k×). EDX spectra were acquired from two selected areas (Spectrum 1 and Spectrum 2); the software quantified only Zn and O, so reported percentages are normalised to these two elements. TEM, HRTEM and SAED were performed on a JEOL JEM-2100 operated at 200 kV; particle diameters were measured directly on the micrograph, and TEM–EDX was acquired from the supported sample.

3. RESULTS AND DISCUSSION

3.1 Formation of the product

The zinc acetate solution was colourless and the extract light green. After pH adjustment to 10–11 and heating, a whitish suspension formed. This indicates precipitation of $Zn(OH)_2$ and its conversion to ZnO but is not diagnostic of ZnO on its own, so the phase was identified from the spectroscopic and diffraction data below. Because the zinc was precipitated with NaOH, Zn(II) remained in the +2 state throughout; the phytochemicals are therefore expected to act through complexation of Zn^{2+}, adsorption on the growing particles and steric stabilisation, and not through electron donation (reduction).

3.2 UV–Visible spectroscopy and optical band gap

The absorbance (Fig. 2a) rises steeply below about 300 nm, shows weak shoulders near 247 and 279 nm, a further shoulder at about 340–380 nm, and falls to a low, featureless level above about 450 nm. The negligible absorbance in the visible region is typical of a wide-band-gap oxide. ZnO nanoparticles usually show an excitonic band-edge absorption near 360–380 nm; here this appears as a broad shoulder rather than a sharp peak, which is consistent with a polydisperse, partly agglomerated sample and with overlapping absorption from organic residues. The shoulders at 247 and 279 nm lie in the region where π→π* transitions of aromatic phytochemicals absorb and are attributed tentatively to residual organic matter. The instrument lamp was changed at 340 nm; a small instrumental step can occur at the changeover wavelength, so the feature at 340 nm is not interpreted as an absorption peak, and the measurement should be repeated with a different changeover wavelength to confirm it.
A Tauc plot for a direct allowed transition (Fig. 2b) gives a linear region between 3.30 and 3.65 eV (R^2 = 0.996) that extrapolates to $E_g \approx 3.18$ eV (3.10–3.22 eV for other reasonable fit windows). This is below the bulk value of ≈3.37 eV. Such narrowing is commonly reported for green-synthesised ZnO and is usually linked to surface defects, hydroxyl groups, and organic residues that create band-tail states; it should not be read as a size effect, because particles of ≈10–20 nm are far above the size range in which quantisation shifts the gap of ZnO. Using absorbance instead of the absorption coefficient, and measuring a dispersion instead of a diffuse-reflectance spectrum of the powder, means the value is an estimate (Makuła et al., 2018).

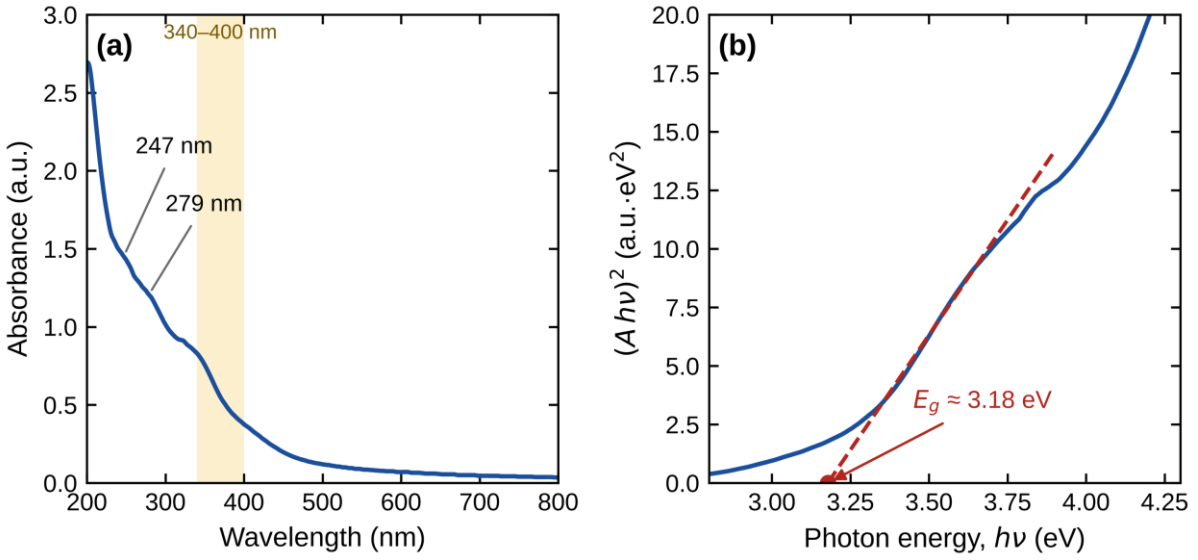


Fig. 2. (a) UV–Vis absorption spectrum of the ZnO nanoparticles (200–800 nm). The shaded band marks the 340–400 nm band-edge region; note the lamp changeover at 340 nm. (b) Tauc plot for a direct allowed transition with the linear fit (dashed) over 3.30–3.65 eV and the extrapolated band gap.

3.3 FTIR spectroscopy

The FTIR spectrum (Fig. 3; Table 1) is dominated by a broad O–H stretching band centred at 3260 cm^{-1} and a very strong, broad band with its minimum at 565 cm^{-1}. The latter is assigned to Zn–O lattice stretching of wurtzite

ZnO, which appears between about 400 and 600 cm^{-1} (Coates, 2000; Kołodziejczak-Radzimska & Jesionowski, 2014). The band at 1634 cm^{-1} is most simply assigned to the H–O–H bending mode of adsorbed water, which also accounts for much of the 3260 cm^{-1} intensity; a contribution from C=O or C=C stretching of residual organic compounds cannot be excluded. The weak bands at 1366 and 1216 cm^{-1} may arise from O–H or C–H bending or symmetric COO^- stretching of residual acetate/carboxylate groups and from C–O stretching of phenolic, alcoholic or ester groups. The very weak feature at 2115 cm^{-1} (96% transmittance) is not interpreted; it lies in a region where cumulated-bond vibrations, ATR crystal, or atmospheric artefacts can appear.

These bands show that hydroxylated, partly organic-covered surfaces are present, which agrees with the oxygen-rich EDX results (Section 3.6). They do not, however, identify specific phytochemicals, since the same bands arise from water and hydroxyl groups. Attributing them to capping agents would require the FTIR spectrum of the dry extract and of ZnO prepared without extract for comparison, which were not measured here.

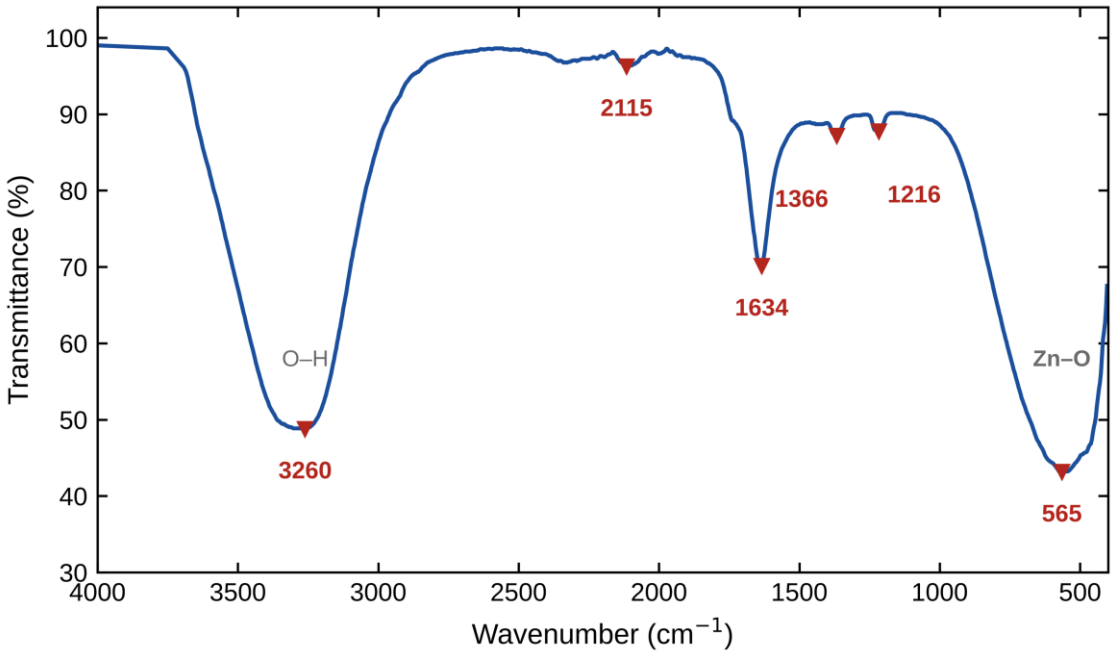


Fig. 3. FTIR spectrum of the ZnO nanoparticles (4000–400 cm^{-1}) with band positions in cm^{-1}.

Table 1. FTIR bands of the ZnO nanoparticles and their assignment.

Band (cm^{-1})	Transmittance (%)	Intensity	Assignment
3260	48.7	strong, broad	ν(O–H) of surface hydroxyl groups and adsorbed water (alcoholic/phenolic O–H may contribute)
2115	96.3	very weak	Not assigned (possible artefact or overtone)
1634	69.9	medium	δ(H–O–H) of adsorbed water; possible C=O/C=C of residual organics
1366	≈87	weak	δ(O–H)/δ(C–H) or $\nu_s(COO^-)$ of residual acetate/carboxylate
1216	87.7	weak	ν(C–O) of phenolic, alcoholic or ester groups
565	43.0	very strong, broad	ν(Zn–O) of wurtzite ZnO

Transmittance values are those at the band minimum (from the instrument peak table; the 1366 cm^{-1} value is read from the spectrum).

3.4 X-ray diffraction

All reflections in the XRD pattern (Fig. 4) can be indexed to hexagonal wurtzite ZnO (space group $P6_3mc$; JCPDS 36-1451): (100), (002), (101), (102), (110), (103), (200), (112) and (201) between 32° and 70° 2θ, with a very weak (202) feature near 77°. The strong peak at about 68° is the (112) reflection, with the weaker (200) and (201) reflections on either side of it. No distinct reflections of $Zn(OH)_2$, $ZnCO_3$, or zinc acetate were resolved, so the powder is phase-pure to the detection limit of laboratory XRD. A very weak, broad feature near 21–22° and a slight rise in background below 10° were not assigned and are likely to reflect amorphous organic material or the sample holder.

The observed peaks lie about 0.2–0.3° above the reference positions (Table 2). Refinement with a zero-offset term (+0.32°) gives a = 3.257 ± 0.001 Å, c = 5.220 ± 0.002 Å, c/a = 1.603, and a unit-cell volume of 47.94 Å^3, within about 0.3% of the reference values (a = 3.250 Å, c = 5.207 Å); the offset is most probably due to sample-height displacement. The (101) reflection is the most intense, but this is the case for randomly oriented ZnO powder: the intensity ratios of (100), (002) and (101) match the reference (texture coefficients 0.89–1.12 for the seven main reflections), so there is no evidence of preferred growth along any plane.

Peak broadening gives Scherrer crystallite sizes of 7.7–13.1 nm (mean 10.2 ± 1.9 nm over the seven main reflections). Instrumental broadening and lattice strain were not separated (a Williamson–Hall analysis was not meaningful for this data set, $R^2 < 0.1$), so this value is a lower bound for the coherent domain size. It is smaller than the TEM particle sizes (Section 3.7), which indicates that at least some particles are polycrystalline or that strain contributes to the broadening.

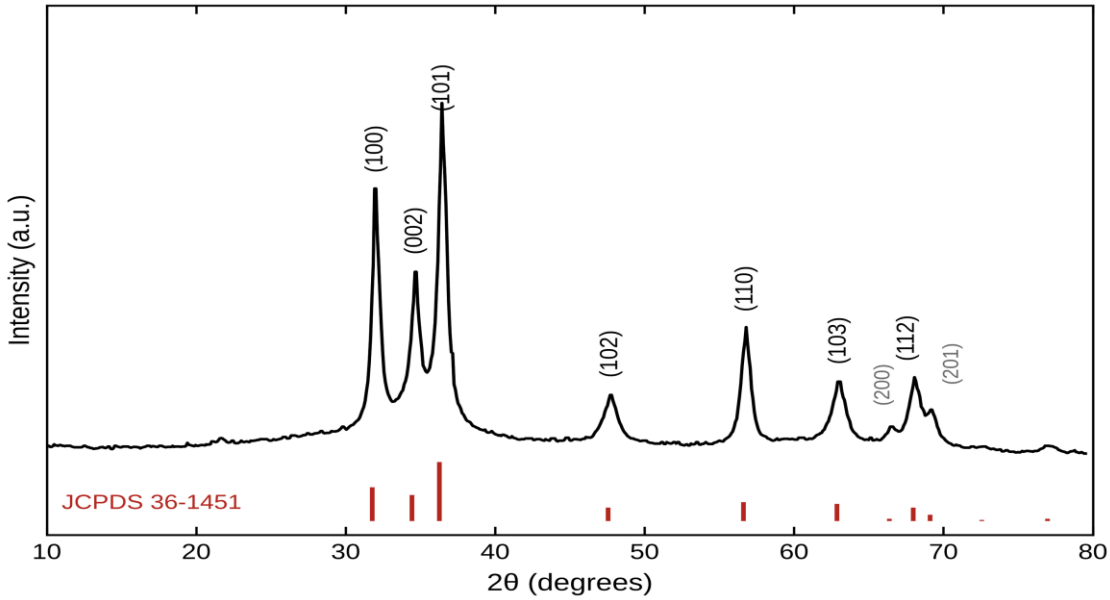


Fig. 4. XRD pattern of the ZnO nanoparticles with Miller indices. Red bars: JCPDS 36-1451 (relative intensities).

Table 2. Indexed XRD reflections, interplanar spacings, and Scherrer crystallite sizes.

(*hkl*)	2θ obs. (°)	2θ ref. (°)	*d*[a] (Å)	*d* ref. (Å)	FWHM (°)	*D* (nm)
(100)	32.03	31.77	2.820	2.814	0.63	13.1
(002)	34.67	34.42	2.609	2.603	0.92	9.0
(101)	36.48	36.25	2.482	2.476	0.73	11.4
(102)	47.74	47.54	1.916	1.911	1.13	7.7
(110)	56.79	56.60	1.628	1.625	0.78	11.6
(103)	63.02	62.86	1.481	1.477	1.07	8.7
(200)	66.57	66.38	1.410	1.407	0.75	(12.7)[b]
(112)	68.09	67.96	1.382	1.378	0.94	10.2
(201)	69.23	69.10	1.362	1.358	0.86	(11.2)[b]

[a] Calculated from the observed 2θ after subtracting the refined zero offset (0.32°). [b] Weak, partly overlapping reflections, excluded from the mean (10.2 ± 1.9 nm). D from the Scherrer equation (K = 0.9, λ = 1.5406 Å, no instrumental correction).

3.5 Scanning electron microscopy

At 200 k× (Fig. 5a), the sample consists of rounded to polyhedral grains whose size, judged against the 100 nm scale bar, is roughly 50–150 nm; the grains are fused into larger clusters with rough, uneven surfaces. At 50 k× (Fig. 5b), these clusters form sub-micrometre agglomerates composed of smaller rounded particles, giving a cauliflower-like texture. Agglomeration is expected for nanoparticles of high surface energy dried from suspension, and the hydroxyl-rich surfaces seen by FTIR can promote it through hydrogen bonding. The grains visible by SEM are therefore secondary particles (aggregates) and are much larger than the 10–20 nm primary crystallites seen by XRD and TEM. SEM does not give a reliable primary-particle size distribution for this sample, and no such distribution is claimed.

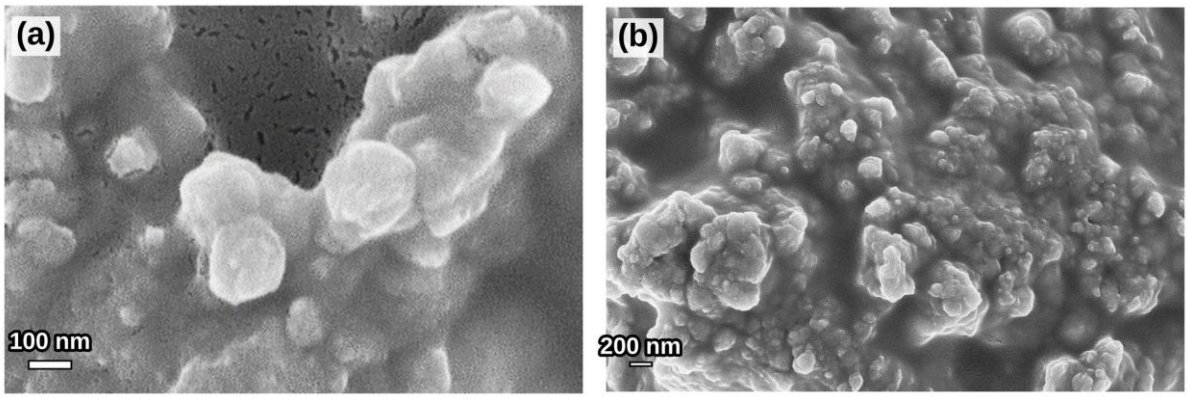


Fig. 5. SEM images of the ZnO nanoparticles at (a) 200 k× and (b) 50 k× (InLens detector, 5.0 kV).

3.6 Energy-dispersive X-ray spectroscopy

The EDX spectra from two areas (Fig. 6) show the Zn L and Zn K lines and the O Kα line. Weak, unlabelled features at about 2 keV and 3.3–3.7 keV (each below roughly 10% of the Zn L intensity) were not assigned or quantified by the software; they may come from the substrate, coating, or residual plant-derived elements and are not interpreted here. Because only Zn and O were quantified, the percentages in Table 3 are normalised to these two elements, and the statement that no other elements are present cannot be drawn from them. Light elements such as carbon are in any case poorly quantified by EDX on rough powders.

Both areas are oxygen-rich relative to stoichiometric ZnO, which contains 80.3 wt.% Zn and 50 at.% Zn. The measured Zn:O atomic ratios are 0.46 and 0.41. The excess oxygen is consistent with surface hydroxyl groups, adsorbed water, and oxygen-containing organic residues (Section 3.3), possible incomplete conversion of $Zn(OH)_2$, and the limited accuracy of EDX for oxygen on non-flat samples. The EDX data therefore confirm that Zn and O are the main elements but do not establish stoichiometric ZnO; the phase assignment rests on XRD.

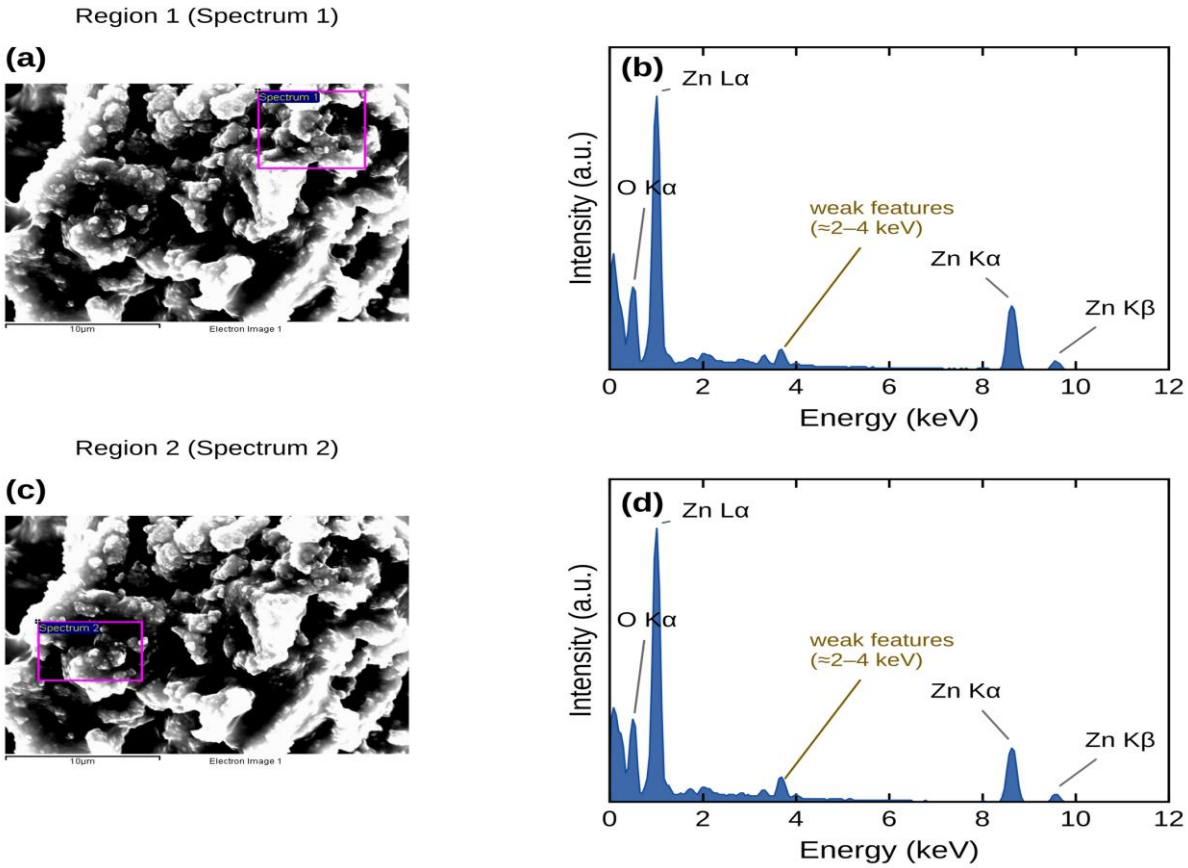


Fig. 6. EDX analysis of two areas. (a, c) SEM images with the analysed regions (magenta boxes; scale bar 10 µm). (b, d) EDX spectra of Spectrum 1 and Spectrum 2 (energy range 0–12 keV; intensities normalised to the Zn L peak).

Table 3. Elemental composition from SEM–EDX (normalised to Zn + O).

Region	Zn (wt.%)	O (wt.%)	Zn (at.%)	O (at.%)	Zn:O (atomic)
Spectrum 1	65.08	34.92	31.32	68.68	0.46
Spectrum 2	62.37	37.63	28.86	71.14	0.41
Stoichiometric ZnO	80.34	19.66	50.00	50.00	1.00

Quantification by the EDX software with only Zn and O included; values for a single acquisition per region.

3.7 Transmission electron microscopy, SAED and TEM–EDX

The TEM overview (Fig. 7a) shows clusters of overlapping nanoparticles. At higher magnification (Fig. 7b), the primary particles are quasi-spherical to polygonal. Seven particles measured directly on this micrograph have diameters of 7.5, 9.6, 10.1, 15.6, 20.7, 20.9 and 22.4 nm (mean 15.3 ± 6.2 nm; Table 4). With only seven particles and a range of 7.5–22.4 nm, the sample cannot be described as having a narrow size distribution; a histogram of at least 100 particles measured with image-analysis software would be needed for that claim. Fringes with a regular spacing are resolved in the lattice image (Fig. 8a), showing that individual particles are crystalline. The lattice fringes show a spacing of about 0.26 nm, consistent with the (002) plane of wurtzite ZnO. The SAED pattern (Fig. 8c) consists of discrete spots arranged around the central beam, as expected for a small number of randomly oriented nanocrystals; it has not been indexed.

The TEM–EDX spectrum (Fig. 8d) is dominated by C Kα, which is attributed to the carbon support film, and shows O Kα and the Zn L lines at low energy. The Zn Kα and Kβ lines at 8.63 and 9.57 keV are barely above the background. Additional peaks at about 6.4 and 8.0 keV are tentatively assigned to Fe Kα and Cu Kα from the specimen holder, pole piece or copper grid, and further minor peaks (e.g., near 4.6, 5.0, and 7.5 keV) were not assigned. TEM–EDX is therefore qualitative only: it confirms the presence of Zn and O but cannot demonstrate purity, and the composition is taken from the SEM–EDX data above.

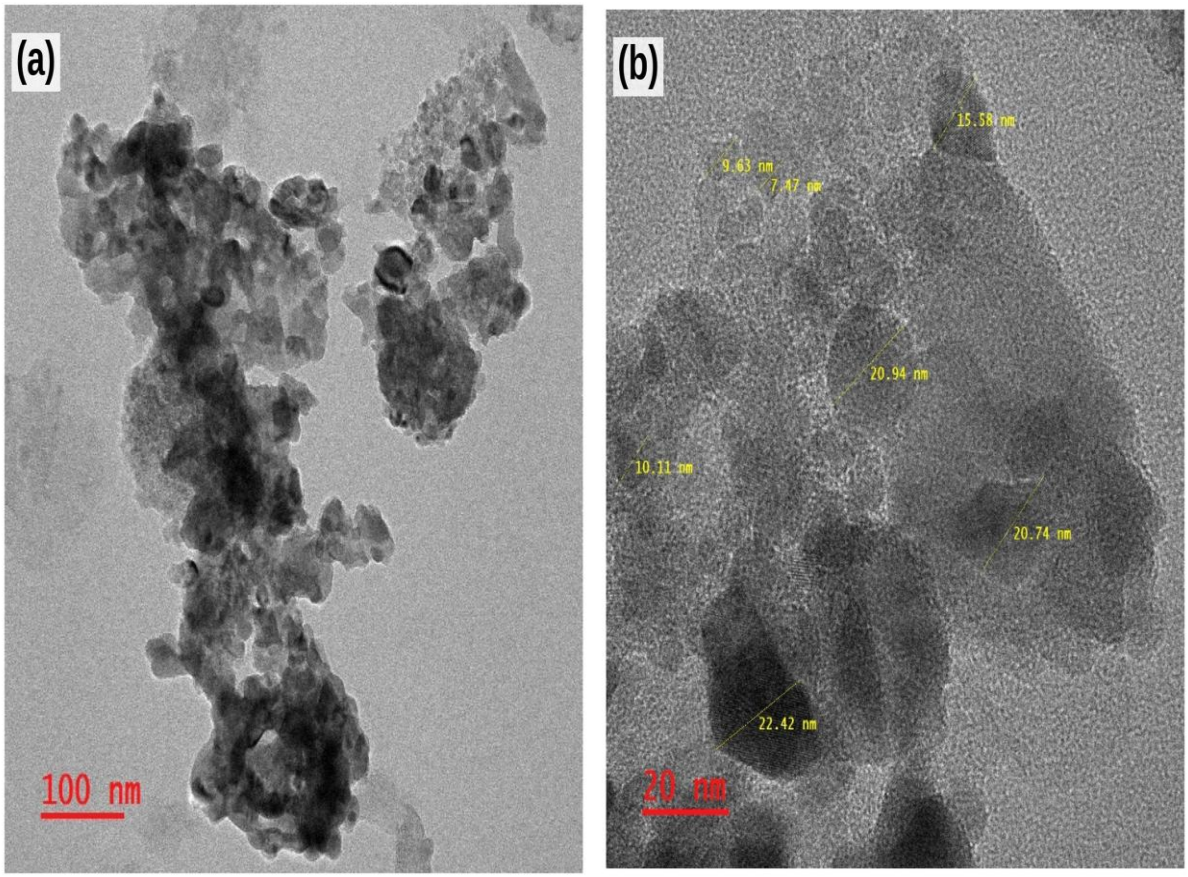


Fig. 7. TEM images of the ZnO nanoparticles: (a) overview (scale bar 100 nm); (b) higher-magnification micrograph with the particle diameters measured (scale bar 20 nm).

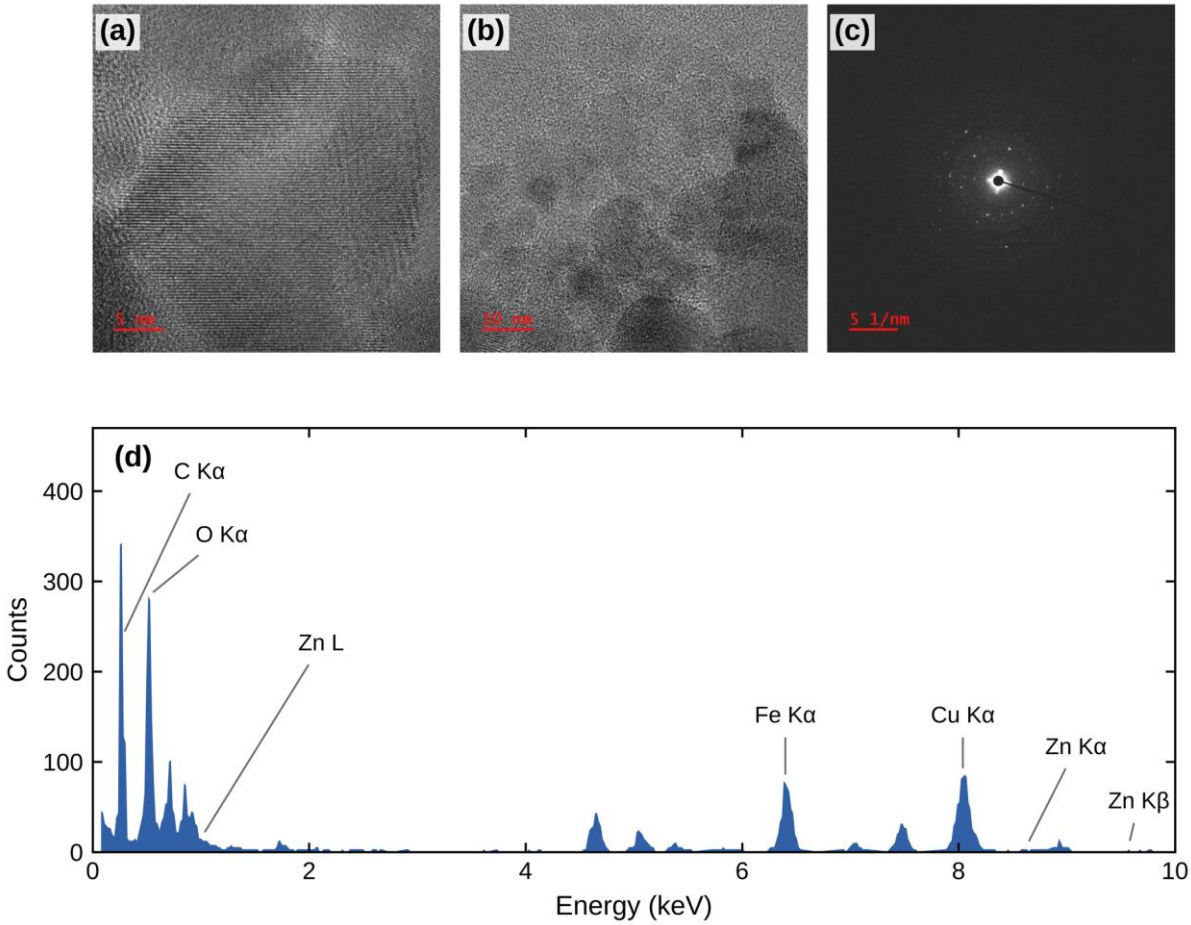


Fig. 8. (a, b) High-resolution TEM images showing lattice fringes (scale bars 5 and 10 nm). (c) SAED pattern (scale bar 5 nm^{-1}). (d) TEM–EDX spectrum; Fe Kα and Cu Kα are tentatively assigned to the holder/grid.

Table 4. Size parameters obtained by different techniques.

Technique	Quantity	Value
XRD (Scherrer)	Coherent domain size (lower bound)	10.2 ± 1.9 nm (7.7–13.1 nm; 7 reflections)
TEM	Primary particle diameter	15.3 ± 6.2 nm (7.5–22.4 nm; n = 7)
SEM	Grains/aggregates	≈50–150 nm grains; sub-micrometre clusters (visual estimate)

Values are mean ± standard deviation. The small TEM sample (n = 7) limits the statistical reliability of the TEM value.

3.8 Consistency across techniques and limitations

The techniques give a consistent picture: XRD shows phase-pure wurtzite ZnO with domains of about 10 nm; TEM shows primary particles of about 8–22 nm that are crystalline; SEM shows that these assemble into agglomerates; FTIR and EDX show a hydroxylated, oxygen-rich, partly organic-covered surface; and the optical band gap (≈3.18 eV) is slightly below the bulk value. The study has the following limitations: the extract was not characterised, and ZnO made without extract was not prepared as a control, so the role of the phytochemicals is inferred, not demonstrated; the number of independent syntheses and measurements is not reported, so batch-to-batch reproducibility is unknown; particle-size statistics rely on seven TEM measurements; and hydrodynamic size, surface charge, surface area, thermal behaviour and photoluminescence (defect emission) were not measured. These limitations should be addressed before application studies such as photocatalysis or antimicrobial testing, which this work does not include.

4. CONCLUSIONS

ZnO nanoparticles were prepared using *Phyllanthus reticulatus* leaf extract by a precipitation–calcination route and characterised by UV–Vis, FTIR, XRD, SEM–EDX and TEM/SAED. XRD confirmed hexagonal wurtzite ZnO (a = 3.257 Å, c = 5.220 Å) with a mean Scherrer crystallite size of about 10 nm and no distinct secondary crystalline phases. The Tauc band gap was ≈3.18 eV, and FTIR showed the Zn–O stretching band at 565 cm^{-1} together with bands from surface hydroxyl groups, adsorbed water and residual organic matter. TEM showed

quasi-spherical, crystalline particles of 15.3 ± 6.2 nm (n = 7) that agglomerate into sub-micrometre clusters seen by SEM, and EDX showed that the samples are oxygen-rich relative to stoichiometric ZnO. Because the particles were formed by NaOH precipitation, the extract acts as a complexing and capping medium and not as a reductant. The data provide a baseline for *P. reticulatus*-derived ZnO; extract and no-extract controls, replicate syntheses, larger particle-size statistics, and surface-area and thermal analyses are the next steps before functional studies.

REFERENCES

1. Agarwal, H., Venkat Kumar, S., & Rajeshkumar, S. (2017). A review on green synthesis of zinc oxide nanoparticles – An eco-friendly approach. *Resource-Efficient Technologies*, *3*(4), 406–413. https://doi.org/10.1016/j.reffit.2017.03.002
2. Ahmed, S., Ahmad, M., Swami, B. L., & Ikram, S. (2016). A review on plant extract-mediated synthesis of silver nanoparticles for antimicrobial applications: A green expertise. *Journal of Advanced Research*, *7*(1), 17–28. https://doi.org/10.1016/j.jare.2015.02.007
3. Altammar, K. A. (2023). A review on nanoparticles: characteristics, synthesis, applications, and challenges. *Frontiers in Microbiology*, *14*, 1155622. https://doi.org/10.3389/fmicb.2023.1155622
4. Coates, J. (2000). Interpretation of infrared spectra, a practical approach. In R. A. Meyers (Ed.), *Encyclopedia of Analytical Chemistry* (pp. 10815–10837). John Wiley & Sons.
5. Iravani, S. (2011). Green synthesis of metal nanoparticles using plants. *Green Chemistry*, *13*(10), 2638–2650. https://doi.org/10.1039/c1gc15386b
6. Kołodziejczak-Radzimska, A., & Jesionowski, T. (2014). Zinc oxide – from synthesis to application: A review. *Materials*, *7*(4), 2833–2881. https://doi.org/10.3390/ma7042833
7. Langford, J. I., & Wilson, A. J. C. (1978). Scherrer after sixty years: a survey and some new results in the determination of crystallite size. *Journal of Applied Crystallography*, *11*(2), 102–113.
8. Luo, S. X., Esser, H. J., Zhang, D., & Renner, S. S. (2011). Nuclear ITS sequences help disentangle *Phyllanthus reticulatus* (Phyllanthaceae), an Asian species not occurring in Africa, but introduced to Jamaica. *Systematic Botany*, *36*(1), 99–104. https://doi.org/10.1600/036364411X553171
9. Makuła, P., Pacia, M., & Macyk, W. (2018). How to correctly determine the band gap energy of modified semiconductor photocatalysts based on UV–Vis spectra. *Journal of Physical Chemistry Letters*, *9*(23), 6814–6817. https://doi.org/10.1021/acs.jpclett.8b02892
10. Mishra, P. K., Mishra, H., Ekielski, A., Talegaonkar, S., & Vaidya, B. (2017). Zinc oxide nanoparticles: a promising nanomaterial for biomedical applications. *Drug Discovery Today*, *22*(12), 1825–1834. https://doi.org/10.1016/j.drudis.2017.08.006
11. Mourdikoudis, S., Pallares, R. M., & Thanh, N. T. K. (2018). Characterization techniques for nanoparticles: comparison and complementarity upon studying nanoparticle properties. *Nanoscale*, *10*(27), 12871–12934. https://doi.org/10.1039/C8NR02278J
12. Mugheri, M. H., Channa, N. A., Rajar, A. B., & Tunio, A. A. (2023). Analysis of phytochemicals in different parts of *the* medicinal plant. *Rawal Medical Journal*. https://www.researchgate.net/publication/373632173
13. Özgür, Ü., Alivov, Y. I., Liu, C., Teke, A., Reshchikov, M. A., Doğan, S., Avrutin, V., Cho, S.-J., & Morkoç, H. (2005). A comprehensive review of ZnO materials and devices. *Journal of Applied Physics*, *98*(4), 041301. https://doi.org/10.1063/1.1992666
14. Patterson, A. L. (1939). The Scherrer formula for X-ray particle size determination. *Physical Review*, *56*(10), 978–982.
15. Sahana, A., Bajpai, S., & Ahirwar, P. (n.d.). Phyllanthus reticulatus – An important medicinal plant and its pharmacological properties. International Journal of Pharmaceutical Research and Applications, 8, 648. https://doi.org/10.35629/7781-08026486532024
16. Sangeetha, S., Krishnamoorthy, K., Panneerselvam, C., & Alasmari, A. (2026). Biogenic ZnO nanoparticle synthesis using *Phyllanthus urinaria* and its multifaceted bioactivities against infection, inflammation, and diabetes mellitus. *Measurement: Food*, *21*, 100267. https://doi.org/10.1016/j.meafoo.2025.100267
17. Shaba, E. Y., Jacob, J. O., Tijani, J. O., & Suleiman, M. A. T. (2021). A critical review of synthesis parameters affecting the properties of zinc oxide nanoparticles and their application in wastewater treatment. *Applied Water Science*, *11*(2), 48. https://doi.org/10.1007/s13201-021-01370-z
18. Sirelkhatim, A., Mahmud, S., Seeni, A., Kaus, N. H. M., Ann, L. C., Bakhori, S. K. M., Hasan, H., & Mohamad, D. (2015). Review on zinc oxide nanoparticles: Antibacterial activity and toxicity mechanism. *Nano-Micro Letters*, *7*(3), 219–242. https://doi.org/10.1007/s40820-015-0040-x
19. Tauc, J., Grigorovici, R., & Vancu, A. (1966). Optical properties and electronic structure of amorphous germanium. *Physica Status Solidi (b)*, *15*(2), 627–637.
20. **********